RESEARCH ARTICLE

NANO · MICRO small
www.small-journal.com

Extra-High Mechanical and Phononic Anisotropy in Black Phosphorus Blisters

Xuwei Cui, Wenlong Dong, Shizhe Feng, Guorui Wang, Congying Wang, Shijun Wang, Yekai Zhou, Xiaohui Qiu, Luqi Liu, Zhiping Xu,* and Zhong Zhang**

Strain is an effective strategy to modulate the electrical, optical, and optoelectronic properties of 2D materials. Conventional circular blisters could generate a biaxial stretching of 2D membranes with notable strain gradients along the hoop direction. However, such a deformation mode cannot be utilized to investigate mechanical responses of in-plane anisotropic 2D materials, for example, black phosphorus (BP), due to its crystallographic orientation dependence. Here, a novel rectangular-shaped bulge device is developed to uniaxially stretch the membrane, and further provide a promising platform to detect orientation-dependent mechanical and optical properties of anisotropic 2D materials. Impressively, the derived anisotropic ratio of Young's modulus of BP flakes is much higher than the values obtained via the nanoindentation method. The extra-high strain-dependent phononic anisotropy in Raman modes along different crystalline orientations is also observed. The designed rectangular budge device expands the uniaxial deformation methods available, allowing to explore the mechanical, and strain-dependent physical properties of other anisotropic 2D materials more broadly.

1. Introduction

Uniaxial strain is an effective knob not only to extract intrinsic mechanical parameters of materials (e.g., Young's modulus, tensile strength, and fracture toughness)[1] but also to modulate the strain-dependent optoelectronic,[2] photonic,[3] magnetic,[4] and catalytic[5] properties of semiconductors. 2D materials (e.g., graphene, hBN, and MoS_2) have achieved enormous attention owing to their atomic layered structures, as well as remarkable chemical and physical properties for fundamental research and potential applications.[6] According to density functional theory (DFT) calculations, there are around 2000 compounds that can be exfoliated in monolayers or multilayers.[7] Among them, anisotropic 2D crystals with low-symmetry structures and in-plane anisotropic properties have become an emerging composition in 2D materials, exhibiting rich and unique low-dimensional physics along crystalline axes. For example, black phosphorus (BP) presents a direct bandgap at all thicknesses, which is advantageous for high-performance electronic and optoelectronic applications.[8] Further, the strain-dependent bandgap of BP makes it an ideal candidate for the development of novel infrared optoelectronic devices.[9] However, owing to its atomic thickness together with extra-low bending rigidity, the application of uniaxial strain in suspended BP remains highly challenging. In addition, although the mechanical and optical properties of BP crystals have been studied, it should be noted that some critical issues have not been solved yet, such as the relatively large discrepancy in Young's modulus between experimental results and theoretical ones.[10] Therefore, from the mechanical point of view, it is fundamentally important to develop a

X. Cui, G. Wang, Z. Zhang
CAS Key Laboratory of Mechanical Behavior and Design of Materials
Department of Modern Mechanics
University of Science and Technology of China
Hefei 230027, China
E-mail: zhongzhang@ustc.edu.cn

X. Cui, W. Dong, C. Wang, S. Wang, Y. Zhou, L. Liu
CAS Key Laboratory of Nanosystem and Hierarchical Fabrication and CAS Center for Excellence in Nanoscience
National Center for Nanoscience and Technology
Beijing 100190, China
E-mail: liulq@nanoctr.cn

W. Dong, C. Wang, Y. Zhou
University of Chinese Academy of Sciences
Beijing 100049, China

S. Feng, Z. Xu
Applied Mechanics Laboratory, Department of Engineering Mechanics and Center for Nano and Micro Mechanics
Tsinghua University
Beijing 100084, China
E-mail: xuzp@tsinghua.edu.cn

X. Qiu
CAS Key Laboratory of Standardization and Measurement for Nanotechnology and CAS Center for Excellence in Nanoscience
National Center for Nanoscience and Technology
Beijing 100190, China

The ORCID identification number(s) for the author(s) of this article can be found under https://doi.org/10.1002/smll.202301959

DOI: 10.1002/smll.202301959

reliable approach to detect the mechanical and strain-dependent physical properties of anisotropic 2D materials.

Analogous to a piece of paper, rich deformation modes such as wrinkles,[11] buckles,[12] tents,[13] folds,[14] and scrolls[15] have been frequently observed in 2D materials in response to mechanical stimuli. However, the nonuniform, highly localized strain distribution, complex deformation modes, as well as lack of tunability within the whole 2D sheet greatly hinder its application. Instead, substrate-assisted deformation becomes one of the most widely utilized strategies to exert uniaxial strains onto 2D materials, in which 2D materials are often transferred onto a flexible substrate, followed by mechanical stretching/compressing/bending.[16] However, it is worth noting that the mechanical deformation of 2D materials was mainly governed by the interface mechanics between the 2D material and supporting substrate,[17] leading to a nonuniform strain distribution within the whole 2D sheets. Therefore, direct mechanical stretching of suspended 2D materials has become a suitable means to explore the intrinsic mechanical parameters of 2D materials.[18] Micromechanical devices, such as push-to-pull (PTP) devices, were utilized to measure Young's modulus, tensile strength, and fracture toughness of graphene, MoS_2, hBN, etc.[1] However, such in situ tensile tests were mainly performed in scanning electron microscopy (SEM)/transmission electron microscopy (TEM) chambers, which would further limit their exploration, especially in the strain engineering field. To the best of our knowledge, it remains a challenge to realize the uniaxial tensile deformation on suspended 2D materials in an atmospheric environment.

Bulge device has been a reliable yet facile way to generate a biaxial strain field to measure the elastic mechanical properties of ultrathin 2D materials, such as Young's modulus and bending rigidity, as well as interfacial parameters.[19] Meanwhile, the biaxial strain feature of 2D blisters offers an efficient way to tailor the band gap of transition metal dichalcogenide (TMD) materials,[16,20] control surface potential distribution,[21] monitor plasmon propagation,[22] and evaluate the Grüneisen parameters of graphene,[23] MoS_2, and VS_2.[24] However, for low-symmetry anisotropic 2D materials, such as $ReSe_2$, the bandgap response to mechanical strain is particularly sensitive to the loading direction.[25] Specifically, the strain along the *a*-direction induces an indirect bandgap of ReS_2 while the strain along the *b*- or *c*-direction does not.[26] Expectedly, the biaxial deformation of conventional bulge devices would greatly weaken the direction-dependent physical responses in anisotropic 2D materials. Therefore, uniaxial stretching is fundamentally important to unveil the dependence of physical properties on crystalline orientations, especially for anisotropic 2D crystals.

Here, motivated by the conventional circular bulge test, rectangular microwells with a certain aspect ratio are designed to achieve the uniaxial in-plane stretching of suspended 2D materials. We employ a typical anisotropic 2D material, BP as a reference, to measure its anisotropic Young's modulus. Owing to its uniform strain distribution, the derived in-plane anisotropy factor of BP is consistent well with the theoretical value (≈3.81).[27] Furthermore, we systematically investigate the strain-dependent Raman responses of BP sheets, revealing their extra-large phononic anisotropy.[28] Our work not only proposes a universal method to extract Young's modulus of anisotropic 2D materials but also offers a novel strategy to detect strain-related electrical, optical, and optoelectronic properties of 2D materials for strain engineering applications.

2. Results and Discussion

2.1. Design of Bulge Device

Figure 1A presents a schematic drawing of the bulge device with a single rectangular hole, in which nitrogen gas was employed as the loading source to push the suspended membrane upwards. In our apparatus setup, Δp reflects the pressure difference across the BP sheet, where $\Delta p = p_0 - p_e$; p_0 and p_e are applied and external atmosphere pressures, respectively. To well control the bulging process, a series of pressure differences were performed across the thin membrane. Meanwhile, an in situ atomic force microscope (AFM) was employed to record the height profile of each blister at a given Δp. Based on classical elastic theory, a membrane with a relatively large length (2*b*)/width (2*a*) ratio ($\frac{b}{a}$) is treated as a long membrane.[29] Figure 1B and Figures S1 and S2, Supporting Information, show the in-plane stress responses of the suspended membranes with different $\frac{b}{a}$ ratios ranging from 1 to 8 based on finite element simulation.[30] Clearly, in the case of $\frac{b}{a} \geq 5$, the stress ratio ($\frac{\sigma_x}{\sigma_y}$) is close to the analysis of long membrane $\frac{1}{\nu}$, where σ_x and σ_y are the stress along the *x* axis and the *y* axis, respectively; ν is Poisson's ratio. Therefore, the thin membrane suspended in the rectangular hole would experience uniaxial tensile stretching along the short axis. Figure S3, Supporting Information, shows the SEM image of the bulge device (5 × 5 mm) with a hole size of 1.8 × 9.0 μm in the silicon nitride/silicon substrate. The BP sample was mechanically exfoliated onto a polydimethylsiloxane (PDMS) substrate and then transferred to the bulge device to fully cover the hole. Figures 1C,D present a typical optical image and AFM height image of the BP flake deposited onto a bulge device, respectively. The thickness and the layer number of BP flakes were identified by AFM as shown in Figure S4, Supporting Information. In particular, to prevent the degradation of BP flakes, the sample preparation and transfer process were conducted in a glove box. Both AFM and micro-Raman spectroscopy characterizations were carried out in a homemade nitrogen chamber.

2.2. Determine the Orientation of BP Crystal

In an atomic-layer BP crystal, each phosphorous atom is covalently bonded to three neighbors via sp^3 hybridization, thus resulting in a pyramid structure with a ridge along the zigzag (ZZ) direction and a pucker along the armchair (AC) direction as presented in **Figure 2**A. Angle-resolved polarized Raman spectroscopy (ARPRS) is a convenient method to determine the crystalline orientation of BP crystals.[31] Figure 2B shows the dependence of the intensity of Raman A_g and $B_g$modes of BP flakes on crystalline orientation, in which three typical Raman modes, namely A_g^1, B_{2g}, and A_g^2, are revealed at 362, 440, and 468 cm^{-1}, respectively. Prior works have pointed out the switching phenomenon of the main axes of the A_g^1 and A_g^2 modes between AC and ZZ directions, as a result of the varied sample thicknesses,

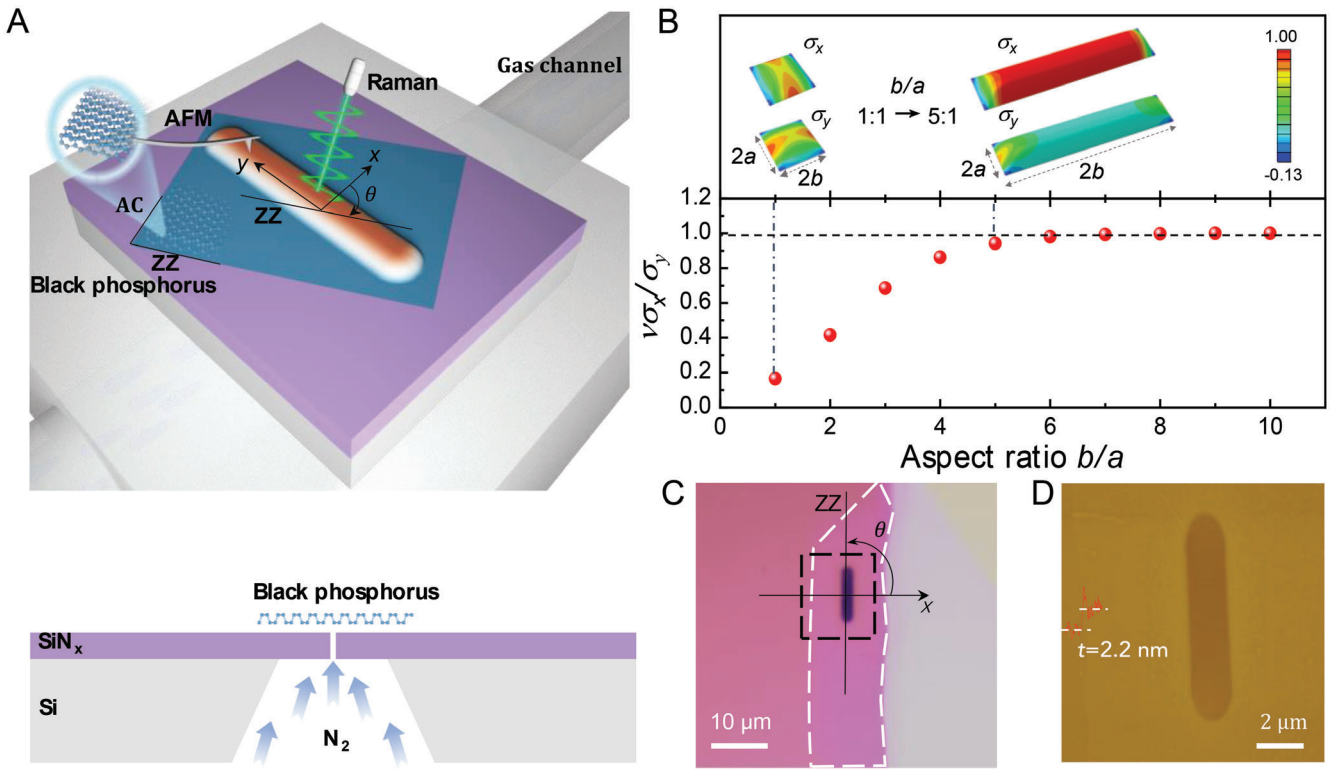

Figure 1. A) Schematic diagram of the rectangular bulge device for uniaxial stretching. B) The lower panel represents the ratio of $\frac{\nu\sigma_x}{\sigma_y}$ at the center against the aspect ratio ($\frac{b}{a}$) of the rectangular hole. The upper panel shows the normalized stress distribution with aspect ratios 1 and 5, respectively. C) Optical image of a few-layer BP flake fully over the hole. D) AFM height image of the dashed region in (C).

and excitation wavelengths, which would further complicate the identification of crystalline orientations of BP crystals.[31,32] More recently, the Raman peak intensity ratio in terms of a concise inequality $I^{AC}_{A^2_g}/I^{AC}_{A^1_g} > I^{ZZ}_{A^2_g}/I^{ZZ}_{A^1_g}$ was proposed to distinguish the AC and ZZ directions of BP crystals.[31] Here, we employed two analysis methods to identify the crystalline orientation of the BP crystals. Figure 2D shows the polar plot of the ARPRS response of three A^1_g, B_{2g}, and A^2_g modes collected from the BP region marked by a red dot in Figure 2C. The periodically varied intensity of the A^2_g mode implies that the main axis of the BP sheet is along the AC direction, which is in good agreement with the inequality analysis.

2.3. Bulge Test and Mechanical Analysis of BP Sheet

Based on the conventional circular-shaped bulge device, earlier works have successfully measured the mechanical properties of isotropic 2D crystals (e.g., graphene, MoS_2, and hBN), inducing Young's modulus,[19] bending rigidity,[19] interfacial adhesion energy,[19] and shear stress[19] between 2D crystals and substrates. Following a similar methodology, it is possible to measure the mechanical parameters of anisotropic 2D crystals along different crystalline orientations. Earlier works have indicated that the pretension in the 2D material sheet would complicate the deformed geometry, and further lead to a nonlinear mechanical response.[33] To evaluate the pretension effect on the mechanical response of BP blisters, herein, we record Raman spectra at varied applied pressure differences shown in **Figure 3**. A downward shift of Raman A^2_g mode was observed once Δp increased from 0 to 450 kPa (Figure 3A), indicating its high strain sensitivity. In Figure 3B, at $\Delta p = 0$ kPa, the flat feature of AFM height profile with ≈5 nm depths together with the unvaried peak position of A^2_g mode inside and outside the hole, implies that the pretension plays a negligible role in the present work. Further, in the case of $\Delta p = 450$ kPa, the A^2_g mode exhibits apparent redshifts with constant peak positions within the suspended region, indicating the uniform strain distribution (Figure 3C). In our previous works,[19] an apparent propagation of shear zone at the interface between graphene and SiO_2 substrate was observed once the pressure differences Δp reached a certain value. However, no apparent shear zone was observed even though the pressure differences increased up to 450 kPa (Figure 3D), further implying the strong interfacial interaction between BP and SiN_x substrate. We attribute it to the presence of dangling bonds in the SiN_x substrate, as well as a relatively small pressure difference across the BP membrane.[16,34] Consequently, both the pretension effect and the interfacial shear deformation between the BP sheet and substrate can be neglected during the bulging process.

Figure 4A presents the evolution of the height profiles of the BP blisters along the *x*-axis as a function of the applied pressure

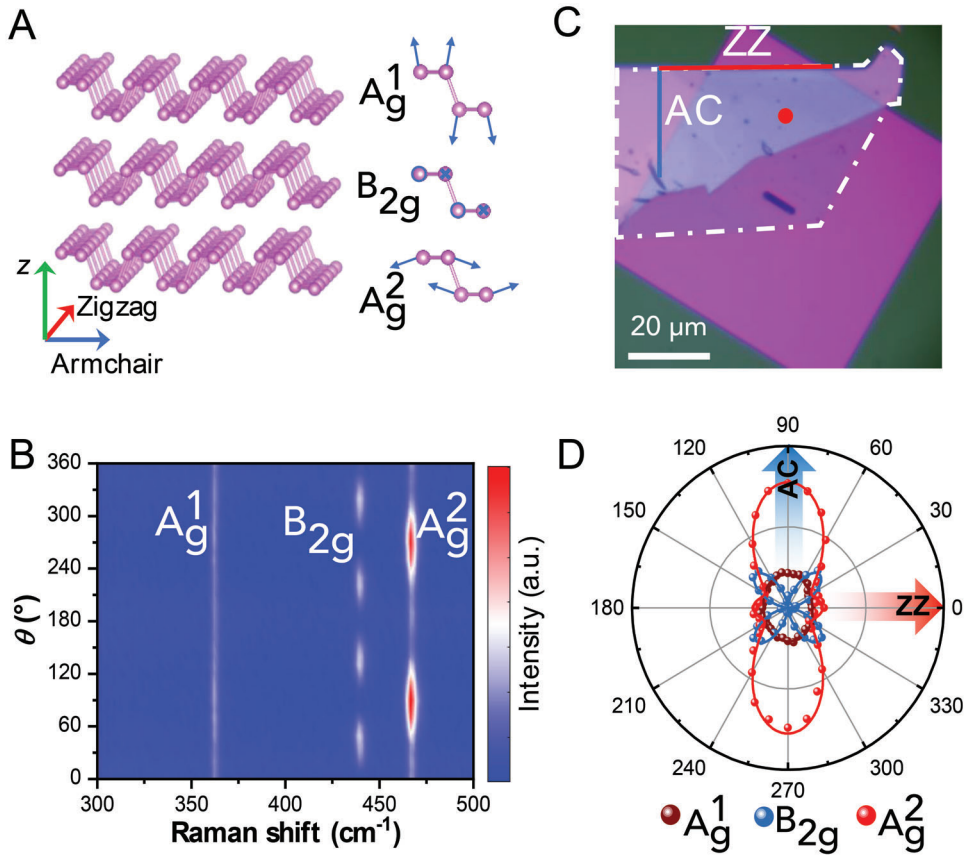

Figure 2. A) Schematic illustration of the anisotropic crystal structure of BP and atomic displacements of the A_g^1, *B2g*, and A_g^2 phonon modes. B) Angle-resolved polarized Raman spectra excited by a 514 nm laser. C) Optical image of a BP flake suspended over a bulge device, where the BP flake is outlined by a dot-dashed line. D) Polar plots of the fitted peak intensities of the A_g^1, B_{2g}, and A_g^2 modes as a function of sample rotation angles under the parallel-polarization configuration taken from the red dot in (C).

difference Δp, in which the sample thickness (t) was 6.6 nm. The shape characteristic of the BP blisters could be well explained by the membrane analysis with $\frac{w(x)}{h} = 1 - \frac{x^2}{a^2}$, where $w(x)$ is the out-of-plane deflection profile, h is the blister height (defection at the center), x is the distance from the hole center, and a is half of the width along the short axis. Following the membrane-like behavior of cylindrical blisters, we build the relation between Δp and h, leading to Equation (1)

$$\Delta p a^4 = K\left(\nu_\theta\right) E_\theta t h^3 \tag{1}$$

where E_θ is Young's modulus and ν_θ is Poisson's ratio in the applied strain direction. θ represents the included angle between the applied strain direction and the ZZ direction of the BP crystal. $K(\nu_\theta)$ is a coefficient that depends only on ν_θ, and detailed information is presented in Figure S5, Supporting Information. The detailed mechanical model and derivation can be obtained from Supporting Information. It should be noted that, for 2D crystal blisters with varied shapes (e.g., circular, square, and cylindrical shape), the relationship between Δp and Eth^3/a^4 can be represented by a similar equation.[19,35] Figure 4B displays the mechanical responses of $\Delta p a^4/K(\nu_\theta)$ versus $h^3 t$ for five BP flakes along different crystalline orientations. The dot-dashed lines represent the linear curving fitting results according to Equation (1), where the slope represents Young's modulus of BP flakes. To avoid the thickness effect, we selected the BP flakes with thicknesses ranging from 2.2 to 7.2 nm as measured by AFM under contact mode (Figure S4, Supporting Information). Upon increasing the included angles θ from 2° to 88°, an apparent decreasing trend of Young's modulus from 151.3 ± 0.3 to 39.6 ± 1.2 GPa was observed, demonstrating the mechanical anisotropy in BP crystals. To exclude the bending contribution, the ratio of blister height and the sample thickness is set larger than 5 (Figure S6, Supporting Information). Here, we employ the elastic solution widely utilized in composites to reveal the dependence of Young's modulus (E_θ) of the BP crystals on the arbitrary included angles between strain direction and ZZ direction, as presented by Equation (2)[10]

$$\frac{1}{E_\theta} = \frac{1}{E_{ZZ}}\cos^4\theta + \left(\frac{1}{G_{\text{eff}}} - \frac{2\nu_{zz}}{E_{ZZ}}\right)\cos^2\theta\sin^2\theta + \frac{1}{E_{AC}}\sin^4\theta \tag{2}$$

where E_{ZZ} and E_{AC} are Young's modulus of the BP crystal along the ZZ and AC orientations, respectively; G_{eff} is the in-plane shear modulus; and ν_{zz} is the Poisson's ratio along ZZ orientation. By fitting the experimental data with Equation (2),

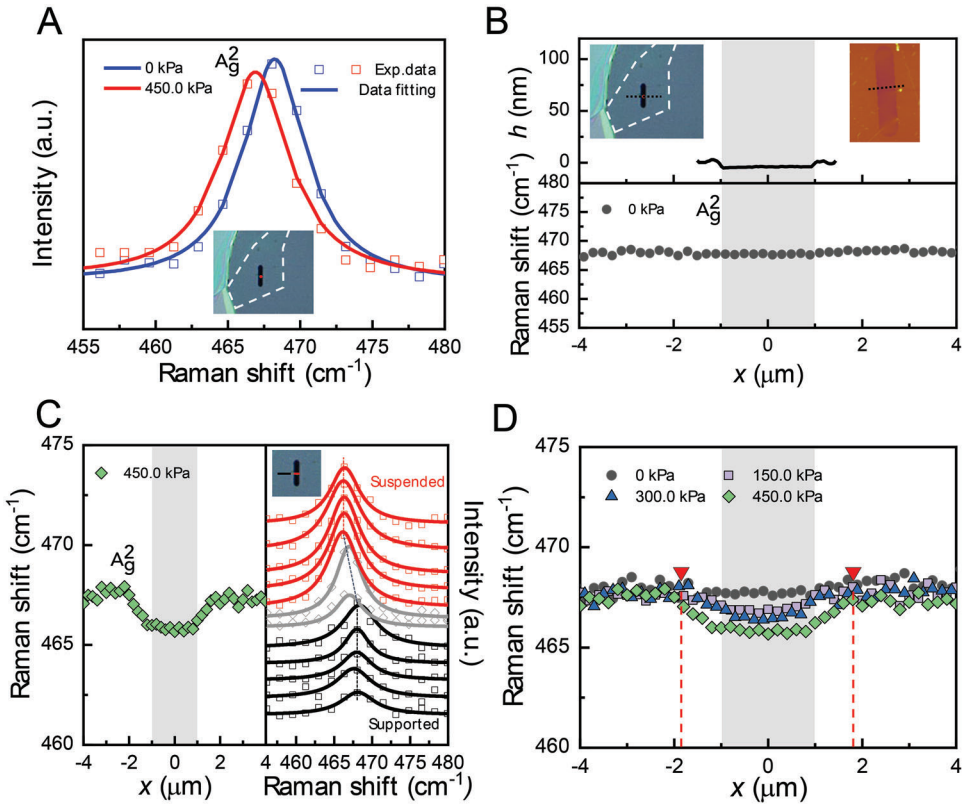

Figure 3. A) Raman A_g^2 mode of BP sheet in response to applied differential pressure. The inset is an optical image of the BP sheet, where the red dot indicates the location at which the Raman measurement was taken. B) AFM height profile of BP sample and the cross-section of Raman contour map of A_g^2 mode at $\Delta p = 0$ kPa. The black dot line in the left insert indicates the location at which AFM and Raman measurements were taken. The right inset shows the AFM height image. C) The cross-section of the Raman contour map of A_g^2 mode at $\Delta p = 450$ kPa and Raman spectra recorded as a function of position. (Top inset) The red curves were recorded from the suspended region (red line position) and the black curves were recorded from the supported region (black line position). The gray curves were recorded from the transition region (gray line located at the edge of the hole). D) A series of the cross sections of Raman contour maps of A_g^2 mode along *x*-axis under different Δp. The red dashed lines indicated the position of Raman A_g^2 peak with zero strain. The gray areas indicate the suspended region of the BP sheet.

eventually, we could obtain the anisotropic Young's modulus of BP crystals along different crystalline orientations. The derived Young's modulus along ZZ and AC directions, and the shear modulus, are E_{ZZ} =151.5 ± 1.1 GPa, E_{AC} = 39.8 ± 1.2 GPa, and G_{eff} = 35.3 ± 3.2 GPa, respectively (Figure 4C). Based on the DFT calculation, we further acquire the theoretical Young's modulus of BP crystals along different crystal directions, which exhibits a similar weakening trend accompanying the orientation switched from the ZZ to AC directions. Impressively, the derived in-plane anisotropy factor of $\frac{E_{ZZ}}{E_{AC}} = 3.81$ is quite close to the theoretical values. Table S1, Supporting Information, summarizes Young's modulus of BP crystals in the literature through AFM nanoindentation and post-buckling methods. Based on previous testing methods, the derived in-plane anisotropy factor was in the range of $2.15 \leq \frac{E_{ZZ}}{E_{AC}} \leq 2.65$, which was much lower than the theoretical results $3.67 \leq \frac{E_{ZZ}}{E_{AC}} \leq 3.87$ (Figure 4E).[10]

Specifically, for AFM based nanoindentation method widely employed in the literature, the testing samples were usually trimmed either by Ar+ plasma or by a focused ion beam to meet the requirement in specific sample geometry.[10c-e] Meanwhile, defects, as well as the residual strain, were unavoidably introduced to the samples, which would further deteriorate the mechanical properties of the BP flake. Furthermore, the effect of sample thickness on Young's modulus has to be taken into concern. Upon exposure to the ambient atmosphere, a significant decrease in elastic modulus for the thinner specimen was widely observed due to layer-by-layer etching.[10d,f,36] Therefore, the multilayer samples with thicknesses ranging from 15 to 151 nm were employed to measure Young's modulus of BP crystals. Such large thickness highlighted the contribution of the bending term to the mechanical response of the BP flake, eventually leading to a relatively lower Young's modulus.[19c,37] In the present work, we mainly employed the samples with thinner thicknesses (ranging from 2.2 to 7.2 nm) to the exclude thickness effect.

Figure 4D shows the 3D AFM images of the BP blister under the same pressure before and after storage for 4 h in the homemade nitrogen chamber. Impressively, there is no apparent change in either blister topography or height profiles. As a demonstration, we have further investigated the evolution of BP flakes in air and homemade nitrogen chamber over time. For BP flake stored in air, an apparent degradation over time was

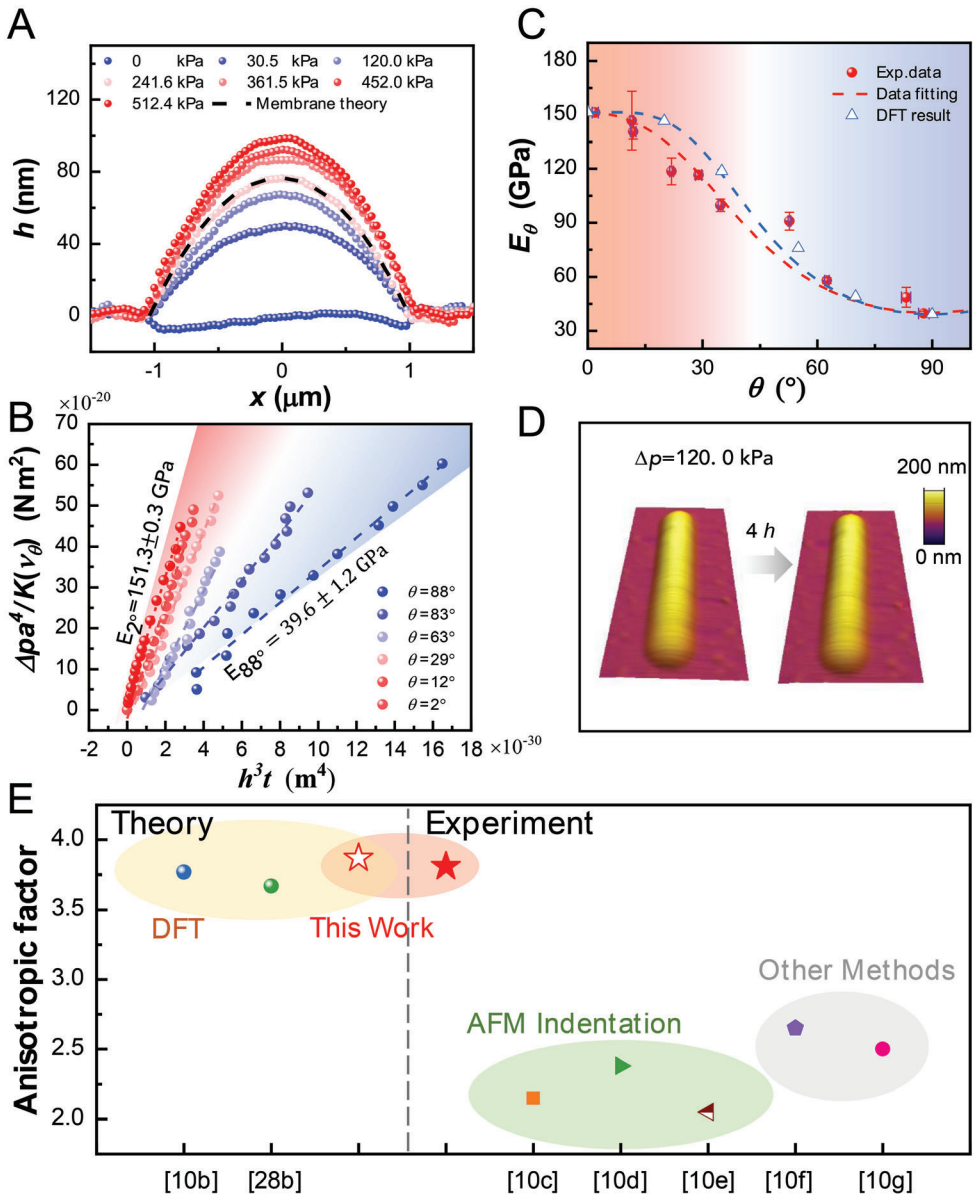

Figure 4. A) Deflection versus position of BP blisters along the *x*-axis under various Δp. The thickness and the angle of the sample are 6.6 nm and θ = 29°, respectively. The dashed black line is obtained from a membrane solution (Equation (S4), Supporting Information). The deflection is measured by AFM. B) $\Delta pa^4/K(\nu_\theta)$ versus h^3t containing six suspended BP sheets with different angles. The slope of the fitting line reflects the corresponding Young's modulus. C) Young's modulus of BP flakes versus different crystal orientations, where 0° and 90° are ZZ and AC orientations, respectively. D) 3D AFM images of the BP blister before and after 4 h storage in the homemade nitrogen chamber. E) Comparison of anisotropic factor ($\frac{E_{ZZ}}{E_{AC}}$) of BP sheet.

captured by AFM characterization (Figure S7, Supporting Information). Instead, for the BP flake stored in a homemade nitrogen chamber, we did not capture any changes, indicating its chemical stability (Figure S7, Supporting Information). Moreover, the repeatable out-of-plane deflections of the BP blister subjected to loading-unloading cycles shown in Figure S8, Supporting Information, further indicates the excellent gas tightness in the bulge device. In a word, as a universal method, the bulge device developed in this work can not only measure the mechanical parameters of anisotropic 2D crystals, but also provide a novel way to explore the rich strain-related phononic, and electrical properties.

2.4. In Situ Raman Response of BP Sheets Under Uniaxial Strain

Prior works have proven that the strain-dependent phonon vibration modes of BP materials in terms of Raman A_g^1, B_{2g}, and A_g^2 modes.[28] The flexible polymeric materials were always employed as supporting substrates to transfer tensile strain to

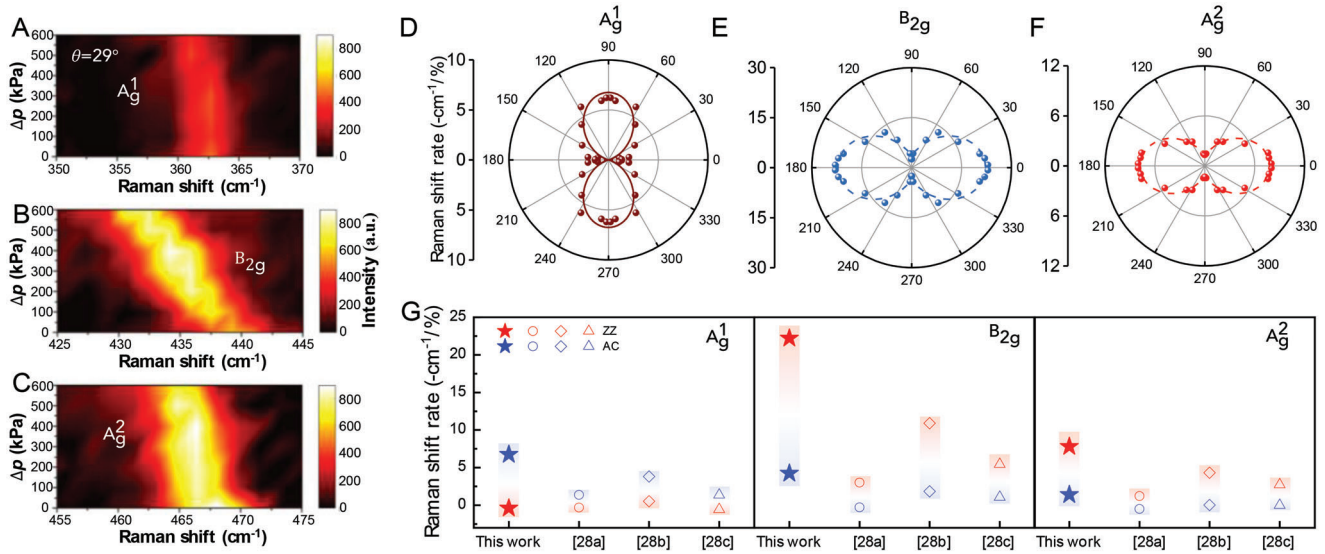

Figure 5. Strain-induced modification of the Raman spectra in BP blisters. Anisotropic Raman responses of A) A_g^1, B) B_{2g}, and C) A_g^2 modes for BP flakes (with $t = 6.6$ nm, $\theta = 29°$) as a function of pressure differences. Polar plot of the angle-dependent Raman shift rates of D) A_g^1, E) B_{2g}, and F) A_g^2 modes of the BP sheets under different uniaxial stretching. G) Comparison of Raman shift rates of three Raman modes.

the individual BP flakes through interfacial shear stress in the spread BP/polymer or sandwiched polymer/BP/polymer structure configurations.[10,16,17] However, owing to the inevitable sliding at the interface during the deformation process, the maximum strain of the BP sheet deformed would be determined by the interfacial shear strength.[17] Specifically, only 20% to 40% of the strain can be effectively transferred to the BP flakes from the polymeric substrate.[28] With the help of the rectangular-shaped bulge device, herein, we could not only directly apply the uniaxial strain to the suspended BP flakes along different crystalline orientations, but also achieve a uniform strain distribution within the whole suspended region. **Figure 5** shows the systematic Raman responses of the characteristic phonon modes, including A_g^1, *B2g*, and A_g^2 of BP flakes, under uniaxial stretching along different crystalline orientations excited by a 514 nm laser in a nonpolarized configuration. The strain can be directly obtained according to $\epsilon = 2h^2/3a^2$, in which h and a are easily obtained from the AFM characterization. Owing to the anisotropic puckered structure of BP, both the shifted trends and rates of specific Raman modes in response to the loading direction become a puzzling issue. In the case of the 6.6 nm BP flake, accompanying the increased pressure difference across the BP flake with the strain direction along $\theta = 29°$, the peak positions of the Raman A_g^1, *B2g*, and A_g^2 modes evolved continuously (Figure 5A–C). Shift rates of specific Raman modes of six BP flakes in response to the uniaxial stretching along the different crystalline orientations with $\theta =$ 2°, 7°, 12°, 29°, 53°, 63°, 83°, and 88°, respectively, are compared in Figure S9, Supporting Information. In the case of stretching direction close to the ZZ direction (Figure S9A, Supporting Information), both Raman B_{2g} and A_g^2 modes show an apparent downward shift with rates of -22.94 and -8.02 cm^{-1}/%, respectively. The high sensitivity of Raman B_{2g} mode can be assigned to the fact that the atomic displacement is mainly along the ZZ orientation. By comparison, the Raman A_g^1 mode is not sensitive to the applied strain along the ZZ orientation (Figure S9, Supporting Information). A similar result with small A_g^1 shift was reported in both experimental and calculated results.[28] Furthermore, once the tensile strain was applied close to the AC direction, the A_g^1 mode switched the shifted trend and reached -6.21 cm^{-1}/%. Meanwhile, for the B_{2g} and A_g^2 modes, the shift rates changed from -22.94 to -2.55 cm^{-1}/% and -8.04 to -1.33 cm^{-1}/%, respectively, in response to a switched loading direction from ZZ to AC directions. The apparent dependence in three phonon modes on the crystallographic orientation further confirms the anisotropic phononic responses of BP crystals. Experimentally, however, it remains challenging to stretch the P–P bonds along the AC or ZZ direction exactly within a single or few atomic layers BP. The deviation with a certain angle between crystalline orientations and strain loading directions was frequently observed in the literature, which results in the complicated trends and variation in shift rates for those characteristic Raman modes in BP crystals. To predict the orientation-dependent Raman shift rates in response to the uniaxial strain for orthorhombic structures (e.g., BP crystals), a theoretical model was employed as presented in Equation (3)[28]

$$K = \frac{\partial \omega}{\partial \varepsilon} = K_{ZZ}\cos^2\theta + K_{AC}\sin^2\theta \quad (3)$$

where K is the Raman shift rate for the tensile direction along θ, K_{ZZ} and K_{AC} are the Raman shift rates along ZZ and AC directions, respectively, ω is the peak position of the Raman band and ϵ is the applied strain. Figure 5D–F shows the polar plots of the shifted rates of three characteristic Raman modes. By fitting the experimental data with Equation (3), we could explain the anisotropic distribution of the phonon modes of BP crystals. Impressively, the maximum values of the derived shifted rates of the B_{2g} and A_g^2 modes could reach -22.20 and -7.79 cm^{-1}/%, respectively, which are much larger than the val-

ues reported in the literature as summarized in Table S2, Supporting Information.[28,38] Meanwhile, as shown in Figure 5G, the suspended BP sheets show giant anisotropic tunable phonon properties, whose range is much larger than reported in the literature. We contributed the observed extra-high sensitivity of phonon modes to the following two aspects:

First, the loading method. Different from the conventional polymeric substrate-assisted deformation method, herein, the uniaxial tensile stretching was directly exerted onto the few-layer BP crystals through the bulge device. The deformation of the BP flakes can be directly measured based on the out-of-plane deflection of the blisters. In comparison, it is hard to derive the real strain of the BP flakes deformed in the polymer-based structure. Furthermore, according to the classic shear-lag theory, the strain of the BP flakes carried is relatively lower than the matrix strain owing to the occurrence of interfacial slippage.[17b,28a] Consequently, the overestimated strain values of the BP flakes would weaken the shift rates of characteristic Raman modes.

Second, the Poisson's ratio (ν) effect. Generally, once the tensile strain is applied along one direction, the sample tends to contract in the perpendicular direction due to the Poisson effect. For long membranes with clamped boundary conditions, the strain along the y-axis was limited ($\epsilon_y = 0$) when it was uniaxially stretched along the x-axis.[29] Consequently, the Poisson's ratio (ν) effect would be ignored because of the restricted lattice contraction perpendicular to the strain direction.

3. Conclusion

In summary, we develop a novel bulge device with a rectangular hole to uniaxially stretch few-layer suspended BP crystals. The extracted Young's modulus in the ZZ and AC directions is 151.5 and 39.8 GPa, respectively. It is the first report that the derived in-plane anisotropy factor of $\frac{E_{ZZ}}{E_{AC}} = 3.81$ aligns well with the theoretical one as predicted by DFT. The extra-high anisotropy in strain-dependent Raman responses further confirms the advantage of the uniaxial stretching of free-standing BP sheets. The developed bulge device is expected not only to be a universal approach for measuring mechanical parameters of 2D materials, but also to provide a promising platform to modulate the strain-dependent optical, electrical, and optoelectronic responses of 2D materials.

4. Experimental Section

Sample Preparation: Bulk BP was purchased from HQ Graphene. The few-layer BP flakes were first micro-mechanically exfoliated onto a PDMS stamp, and then transferred to seal the rectangular hole on a SiN_x/Si substrate. The bulge devices included two parts: a patterned SiN_x/Si substrate and a pressure unit. A digital pressure gauge and a gas flow controller allowed the accuracy of pressure control at 0.1 kPa and the upper limit of pressure at 600 kPa. All operations were carried out in a nitrogen environment.

In Situ Micro-Raman Spectroscopy: All the Raman spectra of BP flakes were obtained using micro-Raman spectroscopy (Renishaw), which included a 514 nm wavelength laser and a 50× objective lens. APRPS was carried out under a parallel-polarization configuration to characterize the crystallographic orientation of BP crystals. The Raman shift rate measurements were performed under a nonpolarized configuration. The laser power was kept low enough (<100 mμW). The characterizations were carried out in a homemade nitrogen chamber.

In Situ AFM: The MFP-3D AFM was used to characterize the blister morphology and measure the thickness of the BP flakes. The characterizations were carried out in a homemade nitrogen chamber by using AFM tips (OLTESPA OMCL-AC240TS) with tetrahedral geometry, and the nominal tip radius was ≈7 nm.

Supporting Information

Supporting Information is available from the Wiley Online Library or from the author.

Acknowledgements

X.C., W.D., and S.F. contributed equally to this work. This work was jointly supported by the National Natural Science Foundation of China (Grant Nos. 11832010, 11890682, 22072031, 12202430) and the Strategic Priority Research Program of the Chinese Academy of Sciences (CAS) under the Grant No. XDB36000000. The authors thank Z. Dai. and X. Ma for the helpful discussion and comments.

Conflict of Interest

The authors declare no conflict of interest.

Data Availability Statement

The data that support the findings of this study are available from the corresponding author upon reasonable request.

Keywords

anisotropy, black phosphorus, blisters, Raman spectra, Young's modulus

Received: March 7, 2023
Revised: May 31, 2023
Published online:

[1] a) Y. Yang, Z. Song, G. Lu, Q. Zhang, B. Zhang, B. Ni, C. Wang, X. Li, L. Gu, X. Xie, H. Gao, J. Lou, *Nature* **2021**, *594*, 57; b) K. Cao, S. Feng, Y. Han, L. Gao, T. H. Ly, Z. Xu, Y. Lu, *Nat. Commun.* **2020**, *11*, 284.
[2] H. Kim, S. Z. Uddin, D. H. Lien, M. Yeh, N. S. Azar, S. Balendhran, T. Kim, N. Gupta, Y. Rho, C. P. Grigoropoulos, K. B. Crozier, A. Javey, *Nature* **2021**, *596*, 232.
[3] a) X. Yuan, F. Weyhausen-Brinkmann, J. Martín-Sánchez, G. Piredda, V. Křápek, Y. Huo, H. Huang, C. Schimpf, O. G. Schmidt, J. Edlinger, G. Bester, R. Trotta, A. Rastelli, *Nat. Commun.* **2018**, *9*, 3058; b) C. Chen, J. Z. Wu, K. T. Lam, G. Hong, M. Gong, B. Zhang, Y. Lu, A. L. Antaris, S. Diao, J. Guo, H. Dai, *Adv. Mater.* **2015**, *27*, 303.
[4] C. Dhital, Z. Yamani, W. Tian, J. Zeretsky, A. S. Sefat, Z. Wang, R. J. Birgeneau, S. D. Wilson, *Phys. Rev. Lett.* **2012**, *108*, 087001.
[5] K. Yan, T. A. Maark, A. Khorshidi, V. A. Sethuraman, A. A. Peterson, P. R. Guduru, *Angew. Chem., Int. Ed.* **2016**, *55*, 6175.
[6] a) K. S. Novoselov, A. Mishchenko, A. Carvalho, A. H. Castro Neto, *Science* **2016**, *353*, aac9439; b) N. R. Glavin, R. Rao, V. Varshney, E. Bianco, A. Apte, A. Roy, E. Ringe, P. M. Ajayan, *Adv. Mater.* **2020**, *32*, 1904302.
[7] a) K. Choudhary, I. Kalish, R. Beams, F. Tavazza, *Sci. Rep.* **2017**, *7*, 5179; b) N. Mounet, M. Gibertini, P. Schwaller, D. Campi, A. Merkys, A. Marrazzo, T. Sohier, I. E. Castelli, A. Cepellotti, G. Pizzi, N. Marzari, *Nat. Nanotechnol.* **2018**, *13*, 246.

[8] a) L. Li, J. Kim, C. Jin, G. J. Ye, D. Y. Qiu, F. H. da Jornada, Z. Shi, L. Chen, Z. Zhang, F. Yang, K. Watanabe, T. Taniguchi, W. Ren, S. G. Louie, X. H. Chen, Y. Zhang, F. Wang, *Nat. Nanotechnol.* **2017**, *12*, 21; b) F. Xia, H. Wang, Y. Jia, *Nat. Commun.* **2014**, *5*, 4458; c) V. Tran, R. Soklaski, Y. Liang, L. Yang, *Phys. Rev. B* **2014**, *89*, 235319.
[9] G. Zhang, S. Huang, A. Chaves, C. Song, V. O. Ozcelik, T. Low, H. Yan, *Nat. Commun.* **2017**, *8*, 14071.
[10] a) J. W. Jiang, H. S. Park, *Nat. Commun.* **2014**, *5*, 4727; b) Q. Wei, X. Peng, *Appl. Phys. Lett.* **2014**, *104*, 251915; c) J. Tao, W. Shen, S. Wu, L. Liu, Z. Feng, C. Wang, C. Hu, P. Yao, H. Zhang, W. Pang, X. Duan, J. Liu, C. Zhou, D. Zhang, *ACS Nano* **2015**, *9*, 11362; d) H. Chen, P. Huang, D. Guo, G. Xie, *J. Phys. Chem. C* **2016**, *120*, 29491; e) Y. Zhao, G. Zhang, M. H. Nai, G. Ding, D. Li, Y. Liu, K. Hippalgaonkar, C. T. Lim, D. Chi, B. Li, J. Wu, J. T. L. Thong, *Adv. Mater.* **2018**, *30*, 1804928; f) L. Vaquero-Garzon, R. Frisenda, A. Castellanos-Gomez, *Nanoscale* **2019**, *11*, 12080; g) Z. Wang, H. Jia, X. Q. Zheng, R. Yang, G. J. Ye, X. H. Chen, P. X. Feng, *Nano Lett.* **2016**, *16*, 5394.
[11] W. Bao, F. Miao, Z. Chen, H. Zhang, W. Jang, C. Dames, C. N. Lau, *Nat. Nanotechnol.* **2009**, *4*, 562.
[12] S. Yang, C. Wang, H. Sahin, H. Chen, Y. Li, S.-S. Li, A. Suslu, F. M. Peeters, Q. Liu, J. Li, S. Tongay, *Nano Lett.* **2015**, *15*, 1660.
[13] a) Z. Dai, D. A. Sanchez, C. J. Brennan, N. Lu, *J. Mech. Phys. Solids* **2020**, *137*, 103843; b) Z. Dai, Y. Hou, D. A. Sanchez, G. Wang, C. J. Brennan, Z. Zhang, L. Liu, N. Lu, *Phys. Rev. Lett.* **2018**, *121*, 266101.
[14] J. Annett, G. L. W. Cross, *Nature* **2016**, *535*, 271.
[15] X. Cui, Z. Kong, E. Gao, D. Huang, Y. Hao, H. Shen, C.-a. Di, Z. Xu, J. Zheng, D. Zhu, *Nat. Commun.* **2018**, *9*, 1301.
[16] a) Y. Zhang, C. Ma, J. Xie, H. Agren, H. Zhang, *Adv. Mater.* **2021**, *33*, 2100113; b) T. M. G. Mohiuddin, A. Lombardo, R. R. Nair, A. Bonetti, G. Savini, R. Jalil, N. Bonini, D. M. Basko, C. Galiotis, N. Marzari, K. S. Novoselov, A. K. Geim, A. C. Ferrari, *Phys. Rev. B* **2009**, *79*, 205433; c) R. Yang, J. Lee, S. Ghosh, H. Tang, R. M. Sankaran, C. A. Zorman, P. X. Feng, *Nano Lett.* **2017**, *17*, 4568; d) J. Quereda, P. San-Jose, V. Parente, L. Vaquero-Garzon, A. J. Molina-Mendoza, N. Agrait, G. Rubio-Bollinger, F. Guinea, R. Roldan, A. Castellanos-Gomez, *Nano Lett.* **2016**, *16*, 2931; e) H. J. Conley, B. Wang, J. I. Ziegler, R. F. Haglund, Jr., S. T. Pantelides, K. I. Bolotin, *Nano Lett.* **2013**, *13*, 3626.
[17] a) L. Gong, I. A. Kinloch, R. J. Young, I. Riaz, R. Jalil, K. S. Novoselov, *Adv. Mater.* **2010**, *22*, 2694; b) G. Wang, Z. Dai, L. Liu, H. Hu, Q. Dai, Z. Zhang, *ACS Appl. Mater. Interfaces* **2016**, *8*, 22554.
[18] a) M. Goldsche, J. Sonntag, T. Khodkov, G. J. Verbiest, S. Reichardt, C. Neumann, T. Ouaj, N. von den Driesch, D. Buca, C. Stampfer, *Nano Lett.* **2018**, *18*, 1707; b) H. H. Pérez Garza, E. W. Kievit, G. F. Schneider, U. Staufer, *Nano Lett.* **2014**, *14*, 4107.
[19] a) R. J. T. Nicholl, N. V. Lavrik, I. Vlassiouk, B. R. Srijanto, K. I. Bolotin, *Phys. Rev. Lett.* **2017**, *118*, 266101; b) G. Wang, Z. Dai, Y. Wang, P. Tan, L. Liu, Z. Xu, Y. Wei, R. Huang, Z. Zhang, *Phys. Rev. Lett.* **2017**, *119*, 036101; c) G. Wang, Z. Dai, J. Xiao, S. Feng, C. Weng, L. Liu, Z. Xu, R. Huang, Z. Zhang, *Phys. Rev. Lett.* **2019**, *123*, 116101; d) S. P. Koenig, N. G. Boddeti, M. L. Dunn, J. S. Bunch, *Nat. Nanotechnol.* **2011**, *6*, 543.
[20] a) Y. Wang, C. Cong, C. Qiu, T. Yu, *Small* **2013**, *9*, 2857; b) P. Johari, V. B. Shenoy, *ACS Nano* **2012**, *6*, 5449; c) D. Lloyd, X. Liu, J. W. Christopher, L. Cantley, A. Wadehra, B. L. Kim, B. B. Goldberg, A. K. Swan, J. S. Bunch, *Nano Lett.* **2016**, *16*, 5836.
[21] S. Liu, X. Cui, Q. Zhang, W. Shen, J. Du, T. Lin, Y. Wang, M. Wu, L. Gu, Y. Gao, C. Hu, L. Liu, S. Yang, C. Jiang, *Adv. Opt. Mater.* **2023**, *11*, 2202288.
[22] H. Hu, R. Yu, H. Teng, D. Hu, N. Chen, Y. Qu, X. Yang, X. Chen, A. S. McLeod, P. Alonso-Gonzalez, X. Guo, C. Li, Z. Yao, Z. Li, J. Chen, Z. Sun, M. Liu, F. J. Garcia de Abajo, Q. Dai, *Nat. Commun.* **2022**, *13*, 1465.
[23] J. Zabel, R. R. Nair, A. Ott, T. Georgiou, A. K. Geim, K. S. Novoselov, C. Casiraghi, *Nano Lett.* **2012**, *12*, 617.
[24] G. Wang, Z. Zhang, Y. Wang, E. Gao, X. Jia, Z. Dai, C. Weng, L. Liu, Y. Zhang, Z. Zhang, *ACS Appl. Mater. Interfaces* **2021**, *13*, 3040.
[25] Y. Liu, X. Li, Y. Guo, T. Yang, K. Chen, C. Lin, J. Wei, Q. Liu, Y. Lu, L. Dong, C. Shan, *J. Alloys Compd.* **2020**, *827*, 154364.
[26] S. Yu, H. Zhu, K. Eshun, C. Shi, M. Zeng, Q. Li, *Appl. Phys. Lett.* **2016**, *108*, 191901.
[27] a) Z. Yang, J. Zhao, N. Wei, *Appl. Phys. Lett.* **2015**, *107*, 023107; b) S. Appalakondaiah, G. Vaitheeswaran, S. Lebègue, N. E. Christensen, A. Svane, *Phys. Rev. B* **2012**, *86*, 035105.
[28] a) S. Zhang, N. Mao, J. Wu, L. Tong, J. Zhang, Z. Liu, *Small* **2017**, *13*, 1700466; b) Y. Li, Z. Hu, S. Lin, S. K. Lai, W. Ji, S. P. Lau, *Adv. Funct. Mater.* **2017**, *27*, 1600986; c) Y. Du, J. Maassen, W. Wu, Z. Luo, X. Xu, P. D. Ye, *Nano Lett.* **2016**, *16*, 6701; d) W. Zhu, L. Liang, R. H. Roberts, J. F. Lin, D. Akinwande, *ACS Nano* **2018**, *12*, 12512.
[29] S. Timoshenko, *Theory of Plates and Shells*, McGraw-Hill, New York **1959**.
[30] M. Smith, *Dassault Systèmes Simulia Corp* Providence, RI **2009**.
[31] a) J. Kim, J. U. Lee, J. Lee, H. J. Park, Z. Lee, C. Lee, H. Cheong, *Nanoscale* **2015**, *7*, 18708; b) B. Zou, Y. Wei, Y. Zhou, D. Ke, X. Zhang, M. Zhang, C.-T. Yip, X. Chen, W. Li, H. Sun, *Nanoscale Horiz.* **2021**, *10*, 809; c) X. Ling, S. Huang, E. H. Hasdeo, L. Liang, W. M. Parkin, Y. Tatsumi, A. R. T. Nugraha, A. A. Puretzky, P. M. Das, B. G. Sumpter, D. B. Geohegan, J. Kong, R. Saito, M. Drndic, V. Meunier, M. S. Dresselhaus, *Nano Lett.* **2016**, *16*, 2260.
[32] M.-L. Lin, Y.-C. Leng, X. Cong, D. Meng, J. Wang, X.-L. Li, B. Yu, X.-L. Liu, X.-F. Yu, P.-H. Tan, *Sci. Bull.* **2020**, *65*, 1894.
[33] a) C. Lee, X. Wei, J. W. Kysar, J. Hone, *Science* **2008**, *321*, 385; b) T. G. J. Chandler, D. Vella, *J. Mech. Phys. Solids* **2020**, *144*, 104109; c) G. Cao, H. Gao, *Prog. Mater. Sci.* **2019**, *103*, 558; d) Z. Dai, N. Lu, *J. Mech. Phys. Solids* **2021**, *149*, 104320.
[34] Y. Xu, J. Yuan, K. Zhang, Y. Hou, Q. Sun, Y. Yao, S. Li, Q. Bao, H. Zhang, Y. Zhang, *Adv. Funct. Mater.* **2017**, *27*, 1702211.
[35] J. S. Bunch, S. S. Verbridge, J. S. Alden, A. M. van der Zande, J. M. Parpia, H. G. Craighead, P. L. McEuen, *Nano Lett.* **2008**, *8*, 2458.
[36] a) H. Huang, B. Jiang, X. Zou, X. Zhao, L. Liao, *Sci. Bull.* **2019**, *64*, 1067; b) Z. Guo, S. Chen, Z. Wang, Z. Yang, F. Liu, Y. Xu, J. Wang, Y. Yi, H. Zhang, L. Liao, P. K. Chu, X.-F. Yu, *Adv. Mater.* **2017**, *29*, 1703811; c) Y. Huang, J. Qiao, K. He, S. Bliznakov, E. Sutter, X. Chen, D. Luo, F. Meng, D. Su, J. Decker, W. Ji, R. S. Ruoff, P. Sutter, *Chem. Mater.* **2016**, *28*, 8330; d) J. D. Wood, S. A. Wells, D. Jariwala, K. S. Chen, E. Cho, V. K. Sangwan, X. Liu, L. J. Lauhon, T. J. Marks, M. C. Hersam, *Nano Lett.* **2014**, *14*, 6964.
[37] W. Wang, X. Ma, Z. Dai, S. Zhang, Y. Hou, G. Wang, Q. Li, Z. Zhang, Y. Wei, L. Liu, *Adv. Mater. Interfaces* **2022**, *9*, 2101939.
[38] Y. Wang, C. Cong, R. Fei, W. Yang, Y. Chen, B. Cao, L. Yang, T. Yu, *Nano Res.* **2015**, *8*, 3944.